

## Article

# Removal of Fe<sup>3+</sup> Ions from Aqueous Solutions by Adsorption on Natural Eco-Friendly Brazilian Palygorskites

Antonieta Middea <sup>1,\*</sup>, Luciana dos Santos Spinelli <sup>2,3</sup> , Fernando Gomes de Souza Junior <sup>2,3</sup> ,  
Thais de Lima Alves Pinheiro Fernandes <sup>1</sup>, Luiz Carlos de Lima <sup>1</sup>, Vitoria Maria Tupinamba Souza Barthem <sup>4</sup>,  
Otávio da Fonseca Martins Gomes <sup>1,5</sup>  and Reiner Neumann <sup>1,5</sup> 

<sup>1</sup> Centre for Mineral Technology (CETEM), Av. Pedro Calmon, 900, Cidade Universitária, Rio de Janeiro 21941908, Brazil; thais.laf@uol.com.br (T.d.L.A.P.F.); luiz.lima@estacio.br (L.C.d.L.); ogomes@cetem.gov.br (O.d.F.M.G.); rneumann@cetem.gov.br (R.N.)

<sup>2</sup> Institute of Macromolecules, Federal University of Rio de Janeiro, Av. Horácio Macedo, 2030, Cidade Universitária, Rio de Janeiro 21941598, Brazil; spinelli@ima.ufrj.br (L.d.S.S.); fernando\_gomes@ima.ufrj.br (F.G.d.S.J.)

<sup>3</sup> COPPE Nanotechnology Engineering Program, Federal University of Rio de Janeiro, Av. Horácio Macedo, 2030, Cidade Universitária, Rio de Janeiro 21941972, Brazil

<sup>4</sup> Physics Institute, Federal University of Rio de Janeiro, Av. Athos da Silveira Ramos, 149, Cidade Universitária, Rio de Janeiro 21941972, Brazil; vitoria@if.ufrj.br

<sup>5</sup> National Museum of Brazil, Federal University of Rio de Janeiro, Postgraduate Program in Geosciences, Av. Quinta da Boa Vista, S/N Bairro Imperial de São Cristóvão, Rio de Janeiro 20940040, Brazil

\* Correspondence: amiddea@cetem.gov.br



**Citation:** Middea, A.; Spinelli, L.d.S.; de Souza Junior, F.G.; Fernandes, T.d.L.A.P.; de Lima, L.C.; Barthem, V.M.T.S.; Gomes, O.d.F.M.; Neumann, R. Removal of Fe<sup>3+</sup> Ions from Aqueous Solutions by Adsorption on Natural Eco-Friendly Brazilian Palygorskites. *Mining* **2024**, *4*, 37–57. <https://doi.org/10.3390/mining4010004>

Academic Editors: Sossio Fabio Graziano, Rossana Bellopede, Giovanna Antonella Dino and Nicola Careddu

Received: 21 December 2023

Revised: 15 January 2024

Accepted: 18 January 2024

Published: 19 January 2024



**Copyright:** © 2024 by the authors. Licensee MDPI, Basel, Switzerland. This article is an open access article distributed under the terms and conditions of the Creative Commons Attribution (CC BY) license (<https://creativecommons.org/licenses/by/4.0/>).

**Abstract:** This work focuses on the characterization of five palygorskite clays from the Brazilian state of Piauí and their feasibility as eco-friendly adsorbents for the removal of Fe<sup>3+</sup> ions from aqueous solutions. For characterization, we applied the techniques of X-ray diffraction (XRD), X-ray fluorescence (XRF), scanning electron microscopy with energy dispersive spectroscopy (SEM/EDS), size distribution measurements, density measurement by He pycnometry, superconducting quantum interference device (SQUID) magnetometry, Fourier-transform infrared spectroscopy (FTIR), thermogravimetric analysis (TGA/DTA), zeta potential measurement, hydrophobicity determination by contact angle, Brunauer–Emmett–Teller surface area analysis (BET technique) and atomic force microscopy (AFM). Batch experiments were performed in function of process parameters such as contact time and initial concentration of Fe<sup>3+</sup>. The natural palygorskites (Paly) had excellent performance for the removal of Fe<sup>3+</sup> from aqueous solutions by adsorption (around 60 mg/g), and the Langmuir is supposedly the best model fitted the experimental data.

**Keywords:** wastewater; iron removal; palygorskite; adsorption; Langmuir isotherm

## 1. Introduction

Iron is widely used in industry for many purposes, but effluents containing iron require adequate treatment since it is not biodegradable and tends to accumulate in living organisms, causing various diseases and disorders, including digestive problems and brain damage. In drinking water, it can also cause an unpleasant odor and taste along with turbidity [1].

Therefore, removal of Fe<sup>3+</sup> from effluents is very important. There are many methods described in the literature for removal of cations [2–7]. However, methods are often expensive and complicated to perform, so there is a need to develop new methods that are simpler and less expensive. Among these methods, adsorption is cost-effective and simple to perform [8–10]. The adsorption process usually employs natural organic or inorganic materials that are abundant and inexpensive [11,12]. In this regard, palygorskite (Paly) is a low-cost and environmentally friendly natural fibrous silicate clay material with tubular structure and good mechanical strength, thermal stability and hydrophilicity [13–18]. The adsorption

capacity of Paly results from its relatively high surface area and the net negative charge in its structure, which attracts and holds cations such as  $\text{Fe}^{3+}$ , and it is a fibrous hydrated magnesium silicate; its structural formula can be written as  $(\text{OH}_2)_4(\text{OH})_2\text{Mg}_5\text{Si}_8\text{O}_{20}\cdot 4\text{H}_2\text{O}$  [19]. It presents ribbons of 2:1 phyllosilicate units, where each ribbon is connected to the next by the inversion of  $\text{SiO}_4$  tetrahedrons along a set of Si-O-Si bonds, resulting in channels parallel to the phyllosilicate ribbons that contain zeolitic and bound water [20]. Paly deposits around the world mostly come from arid or semiarid regions [21]. In Brazil, these deposits are mainly located in the municipality of Guadalupe, Piauí state (see Figure 1), and were discovered in 1982 [22–27]. Paly has been used in domestic water purification, drilling fluids, cosmetics, pharmaceuticals and polymer formulations [28–36], including to remove cations by adsorption [37–40].

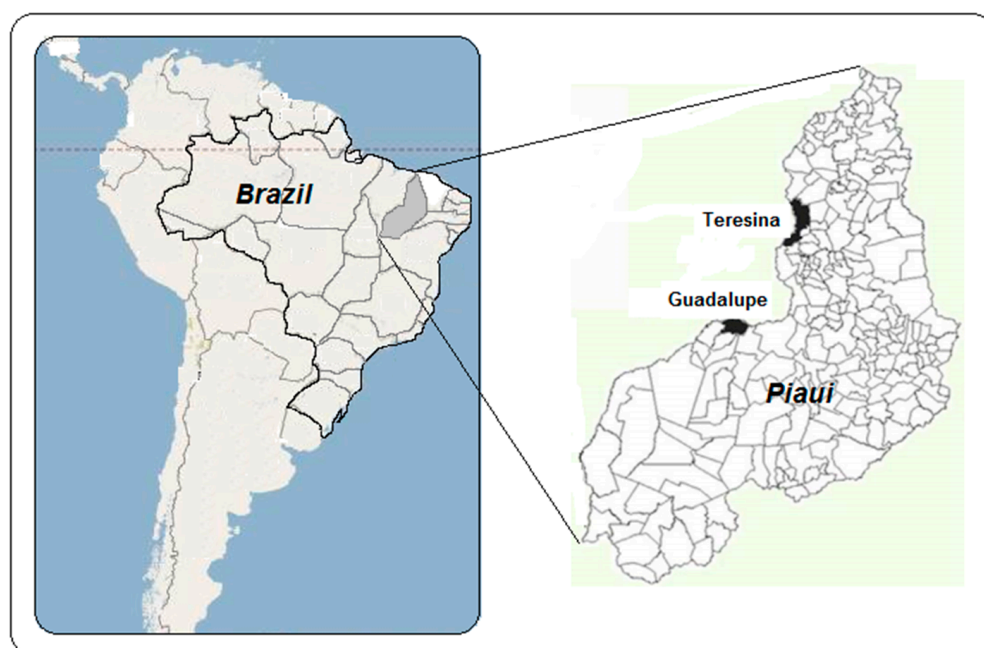


**Figure 1.** Location of the Paly deposits in Guadalupe, Brazil.

In this work, five eco-friendly adsorbents as Palys (Paly I, Paly II, Paly III, Paly IV and Paly V) were used to remove  $\text{Fe}^{3+}$  from an aqueous solution, as a continuation of a previous study where this possibility was investigated [9], being the great novelty of this study. First, the Paly samples were subjected to quartz concentration reduction. After that, they were characterized by XRD, XRF, SEM/EDS, size distribution analysis, density measurement by He pycnometry, SQUID magnetometry, FTIR, TGA/DTA, zeta potential and hydrophobicity by contact angle measurement. Next, adsorption experiments were performed to evaluate the effects of time and initial  $\text{Fe}^{3+}$  concentration. Kinetic and equilibrium models were fitted to the experimental adsorption data to investigate the potential adsorptive influence of Palys on the  $\text{Fe}^{3+}$  removal. The Paly sample with the best iron adsorption performance was further characterized by the BET and AFM techniques.

## 2. Materials and Methods

### 2.1. Materials

The Paly clay deposits used in this work are located in the municipality of Guadalupe, located about 300 km south of the capital of Piauí state, in the North region of Brazil (Figure 1). Regarding the impurities present in the composition of Palys, this depends on the geological formation as well as on the extraction location [41–43].

Paly clays were kindly donated by the company Colorminas-Colorífico e Mineração S.A (Piauí-Guadalupe, Brazil) and were purified by sedimentation and screening. The

particle size was selectivity restricted to below 20  $\mu\text{m}$  by passing the ground purified sample through a 635-mesh sieve.

For this study, 5 Paly samples were selected from a total of 13 samples from different mining areas of the company. The criterion used for this choice was to observe which samples had the highest peaks referring to Paly in the X-ray diffractogram (d-spacing = 10.5  $\text{\AA}$ ). These five Palys were processed using the dense liquid separation technique (bromoform,  $d = 2.89 \text{ g/cm}^3$ ) [44] in order to reduce the quartz concentration in the samples.

Analytic-grade ferric chloride hexahydrate ( $\text{FeCl}_3 \cdot 6\text{H}_2\text{O}$ ) was used as received from Merck, and distilled water (pH 6.0 and <550 ppm of total salt content) was used throughout.

## 2.2. Batch Kinetic Experiments

Batch adsorption experiments were conducted with 100,000 mg/L Paly and initial  $\text{Fe}^{3+}$  concentrations (zero to 20,000 mg/L) ( $C_i$ ) under ambient conditions and carried out in 50 mL conical flasks placed in a thermostatic shaker bath at 130 rpm. The residual concentration ( $C_f$ ) of  $\text{Fe}^{3+}$  after centrifugation at 3500 rpm for 15 min was determined by a LaMotte Smart Spectro UV-VIS spectrophotometer using 1 cm path quartz cells and a wavenumber of 370 nm by comparison with a previously established analytical curve [9].

## 2.3. Adsorption Procedure

The adsorption capacity of  $\text{Fe}^{3+}$  on Palys was calculated through the following equation:

$$\Gamma = (C_i - C_f) \cdot V/W \quad (1)$$

where  $\Gamma$  is the  $\text{Fe}^{3+}$  adsorption capacity of the adsorbent (mg/g),  $C_i$  is the initial concentration of the  $\text{Fe}^{3+}$  solution (mg/L),  $C_f$  is the final  $\text{Fe}^{3+}$  concentration in solution (mg/L),  $W$  is the weight of adsorbent used (g) and  $V$  is the volume of the  $\text{Fe}^{3+}$  solution (L).

## 2.4. Characterization of Materials

### 2.4.1. Mineralogical and Chemical Characterization

The mineralogical analyses of the Paly clays were carried out by XRD. To avoid preferred orientation, the samples were back-loaded and the XRD patterns were obtained with a Bruker-D4 Endeavour diffractometer (Karlsruhe, Germany) operating at a tube voltage and current of 40 kV and 40 mA, respectively, using  $\text{Co } K\alpha$  radiation. Diffraction patterns were recorded between  $5^\circ$  and  $80^\circ$  2 theta with a  $0.02^\circ$  step and a position-sensitive LynxEye detector (Karlsruhe, Germany).

The chemical composition of the samples was determined by XRF after loss on ignition (LOI) determination with a LECO TGA 701 analyzer using a Panalytical AxiosMax spectrometer (Worcestershire, UK) on melted beads (lithium metaborate:tetraborate mixture).

### 2.4.2. SEM/EDS

The morphology and elemental composition of the Palys were carried out using two scanning electron microscopes. The first one observed the morphology of Palys by secondary electrons in an FEI Quanta 400 scanning electron microscope (Hillsboro, OR, USA) operating at 25 kV and small spot size. The second, a Hitachi TM3030Plus (Tokyo, Japan) scanning electron microscope with an integrated energy-dispersive X-ray fluorescence spectrometer (Bruker Quantax 70 from Karlsruhe, Germany) was used for identification of elements present in the Paly samples (coated with Ag), such as magnesium, and the increase in iron content after the process of adsorption. This SEM was operated at 15 kV, small spot size, while images were acquired in backscattered electron mode (BSE) for elemental contrast and EDS maps were used to identify the elements of interest, accumulated during 200 s.

#### 2.4.3. FTIR

The infrared spectra were obtained using a Perkin-Elmer 1720X spectrophotometer (Orpington, UK) in transmission mode. Spectra over the 4000–400  $\text{cm}^{-1}$  range were obtained from 0.01 g of each sample diluted with KBr.

#### 2.4.4. TGA/DTA

The TGA/DTA analysis was performed with a Mettler Toledo TGA/DSC1 Star System (STARe software, version 9.00), at a heating rate of 10  $^{\circ}\text{C}/\text{min}$ , under air atmosphere with a flow rate of 50 mL/min.

#### 2.4.5. Size Distribution and Surface Charge

The size distribution of the five Palys was evaluated by two techniques: laser diffraction with a Mastersizer 2000 analyzer and dynamic light scattering with a Zetasizer Nano ZS, both from Malvern Instruments (Grovewood Road, UK). These techniques allow particle size detections between 0.1  $\mu\text{m}$  and 1000  $\mu\text{m}$  and 0.6 nm and 6  $\mu\text{m}$ , respectively. For these methods, the samples were dispersed in water for 30 min at 1700 rpm.

Surface charges were also evaluated with a Malvern Instruments Zetasizer Nano ZS. For surface charge measurements (an average of 3 points), a suspension of each Paly sample in  $10^{-3}$  molar KCl (indifferent electrolyte) was prepared. The pH was adjusted with NaOH and HCl in the range between 2.0 and 11.0 [21].

#### 2.4.6. Hydrophobicity

The Palys' hydrophobicity was evaluated by water contact angle measurements with a Dataphysics OCA Series goniometer (Filderstadt, Germany), with the Paly and Paly- $\text{Fe}^{3+}$  samples placed on a slide and pressed to form small disks using the sessile drop technique.

#### 2.4.7. Density Measurement by He Pycnometry and BET Surface Area Analysis

The Palys' densities and surface areas were measured with an AccuPyc 1330 (He) pycnometer and an ASAP 2010 analyzer, respectively, from Micrometrics Instrument Corporation (Norcross, GA, USA).

The BET surface area and pore properties of the Paly III sample were determined from  $\text{N}_2$  adsorption–desorption experiments at 77 K using an accelerated surface area and porosimetry system. The sample was outgassed at 70  $^{\circ}\text{C}$  for 24 h to remove any moisture or adsorbed contaminants before the surface area measurements. The microporous surface area, external surface area and the micropore volume were obtained by the t-plot method. Meanwhile, the pore volume and pore-size distribution were estimated by the Barrett–Joyner–Halenda (BJH) method [45].

#### 2.4.8. SQUID Magnetometry

SQUID Cryogenic S600 magnetometer

The magnetic behavior of the samples was observed by the measurements obtained with a magnetometry system based on a physical effect and quantification of the magnetic flux in a closed superconductor circuit, which is highly sensitive to small magnetic flux variations. For these measurements, we used a clear plastic straw as the sample holder because of the negligible magnetic signal in relation to that of the various samples tested.

#### 2.4.9. AFM

Finally, the three-dimensional AFM topographical acquisition image of Paly III crystals was obtained with a JPK atomic force microscope, where the sample was fixed on a transparent glass slide using double-sided adhesive tape. Roughness was measured using the root mean square (RMS) value within the given regions.

### 3. Results and Discussion

#### 3.1. XRD Studies

##### 3.1.1. Quartz Concentration Reduction of Raw Palys

Figure 2 shows the comparison of XRD spectra for raw Palys and Palys after quartz reduction. It can be noted that the quartz diffraction peaks were greatly reduced after using the dense liquid separation technique (Figure 2a–e). Figure 2f shows the quartz XRD intensities of the most significant peak (d-spacing = 3.34 Å) before and after reduction treatment. This enabled an approximate analysis of the amount of quartz phase present in the five Palys, verifying quartz reduction efficiency of around 80%.

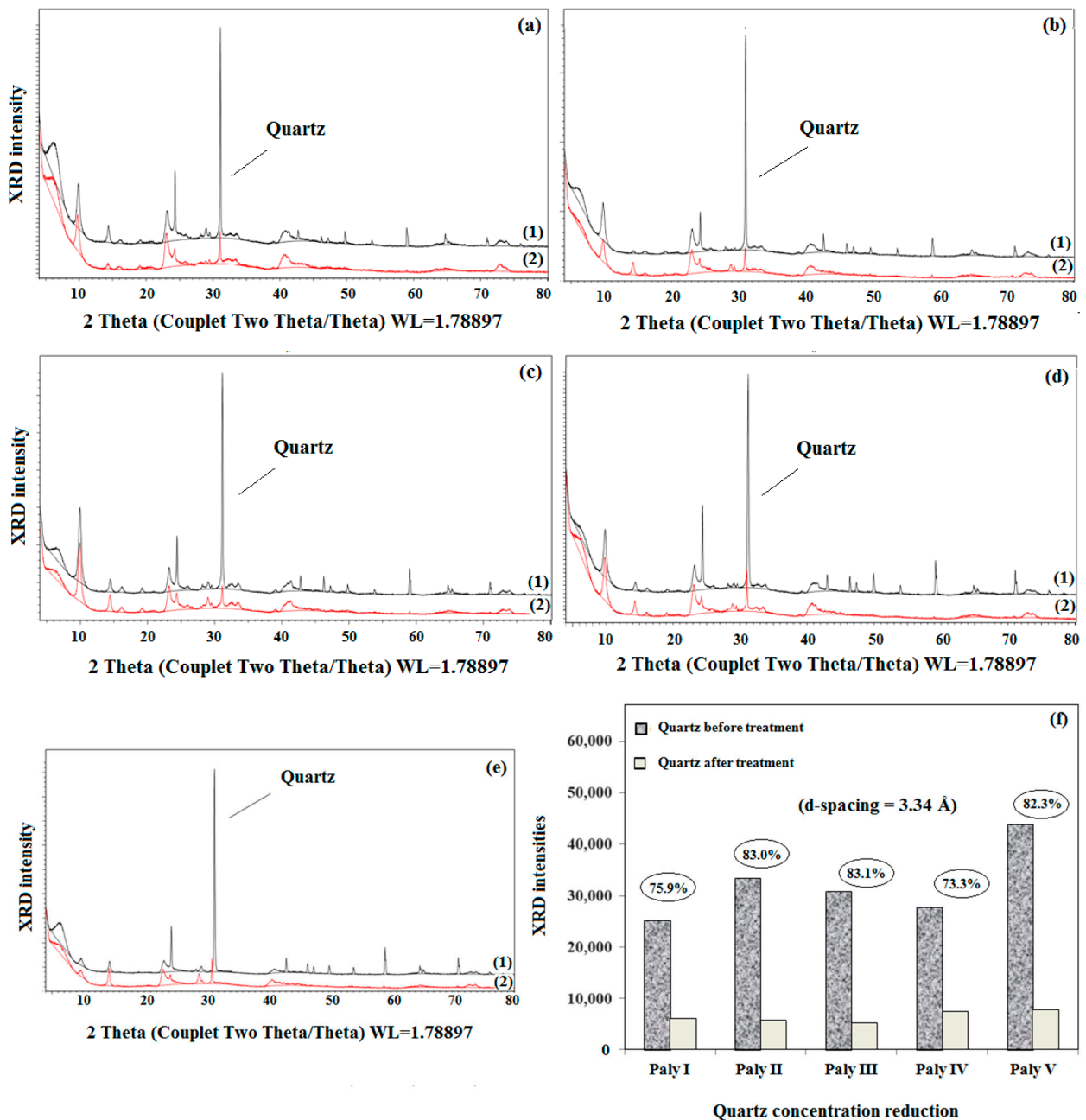


**Figure 2.** X-ray diffraction patterns of Palys before (1) and after (2) reduction of the quartz concentration: (a) Paly I; (b) Paly II; (c) Paly III; (d) Paly IV and (e) Paly V. (f) Quartz XRD intensities of the most significant peak (d-spacing = 3.34 Å) before and after treatment.

### 3.1.2. Mineralogical Analysis

The XRD patterns of the Palys and Palys-Fe<sup>3+</sup> are shown in Figure 3a–e. An identical pattern of the Paly standard can be seen, and their peaks did not undergo significant changes [46]. The impurities found were clinocllore [Fe<sub>6</sub>Si<sub>4</sub>O<sub>10</sub>(OH)<sub>8</sub>], kaolinite [Al<sub>2</sub>Si<sub>2</sub>O<sub>5</sub>(OH)<sub>2</sub>], quartz [SiO<sub>2</sub>], anatase [TiO<sub>2</sub>] and diaspore [AlO(OH)]. The identified crystalline phases were in agreement with the results observed by XRF (Table 1). Additionally, Figure 3f shows a comparison of the XRD count intensities of the main Paly peak (d-spacing = 10.5 Å), indicating that Paly III had a higher concentration than the other samples, which can also be observed by XRF for the MgO content (Table 1).

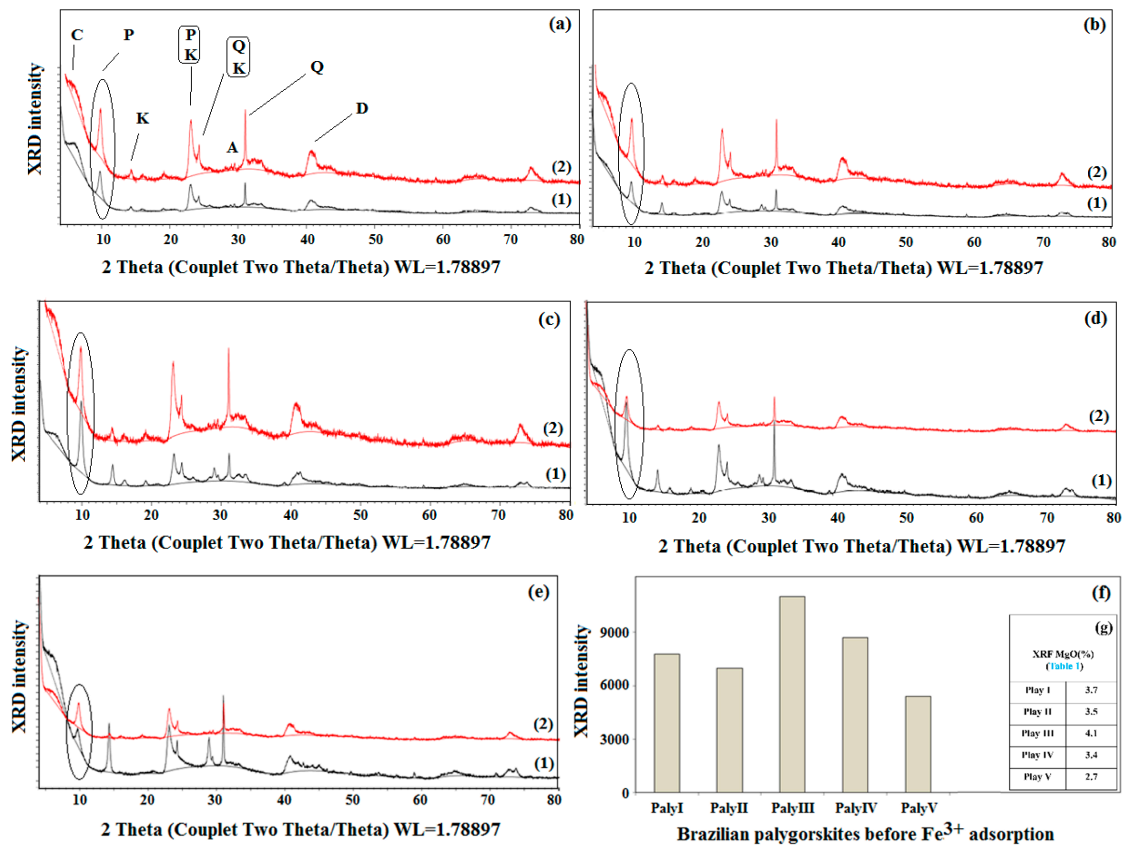


**Figure 3.** X-ray diffraction patterns of Palys before (1) and after Fe<sup>3+</sup> adsorption (2): (a) Paly I; (b) Paly II; (c) Paly III; (d) Paly IV and (e) Paly V. Mineral phases observed: C—clinocllore; P—palygorskite (circles highlighting the main peak of Palys); K—kaolinite; Q—quartz; A—anatase and D—diaspore. (f) Palys XRD intensities of the most significant peak (d-spacing = 10.5 Å) and (g) XRF MgO results from Table 1.

**Table 1.** Chemical composition of Palys before and after adsorption with Fe<sup>3+</sup> by XRF (wt%).

Oxides (%)	Paly I		Paly II		Paly III		Paly IV		Paly V	
	Before	After	Before	After	Before	After	Before	After	Before	After
SiO <sub>2</sub>	51.0	45.4	52.7	47.5	50.7	44.9	49.3	43.8	50.3	44.3
MgO	3.7	3.7	3.5	3.3	4.1	4.1	3.4	3.4	2.7	2.6
Al <sub>2</sub> O <sub>3</sub>	13.1	11.2	15.7	11.9	16.4	12.7	17.2	13.1	17.8	13.8
Fe <sub>2</sub> O <sub>3</sub>	9.8	15.3	8.4	14.6	8.3	14.2	8.5	14.5	10.2	16.1
TiO <sub>2</sub>	1.1	1.1	1.2	1.2	1.7	0.8	1.1	1.0	1.0	1.1
K <sub>2</sub> O	1.6	1.6	1.3	1.3	1.2	1.2	1.6	1.6	1.1	1.1
LOI *	19.7	21.7	17.2	20.2	17.6	22.1	18.9	22.6	16.9	21.0
Total	100	100	100	100	100	100	100	100	100	100

\* LOI (loss on ignition). Highlighted: MgO represents principal palygorskite content and Fe<sub>2</sub>O<sub>3</sub> shows the increase in iron after adsorption.

### 3.2. Characterization of Palys before and after $Fe^{3+}$ Adsorption (Palys- $Fe^{3+}$ )

#### 3.2.1. XRF

XRF data of Palys and Palys- $Fe^{3+}$ , expressed in oxide percentage, are shown in Table 1. The first loss, around 20%, is related to loss of water and organic matter.  $SiO_2$  (above 43%) and  $Al_2O_3$  (around 15%) were the main components found in the Palys, and both concentrations decreased after  $Fe^{3+}$  adsorption, as expected. On the other hand, iron concentration increased in all Palys studied after  $Fe^{3+}$  adsorption, from approximately 9% to 15%.

#### 3.2.2. Microtexture Studies—SEM

The SEM observations verified the characteristic morphology for the five Palys and Palys- $Fe^{3+}$ . The Paly fibers are depicted in Figure 4. Unmodified Palys (Figure 4(1)) show typical fibers, with variable thicknesses and lengths, with randomly oriented shapes in aggregates, as shown in several previous studies [47–50]. This was probably due to strong physical and hydrogen bonding interactions between OH groups of Paly fibers. A large number of crystal beams and a few single needle-like crystals were also observed. The fiber bundles were usually assembled by an individual needle. The morphological differences between the unmodified Palys and Palys- $Fe^{3+}$  can be observed in Figure 4(2), where there were no significant differences after  $Fe^{3+}$  adsorption on Paly surfaces. Finally, Figure 4(3) shows a detailed image of a Paly sample (Paly I), where an individual needle measuring 1.82  $\mu m$  versus 95.2 nm can be observed.

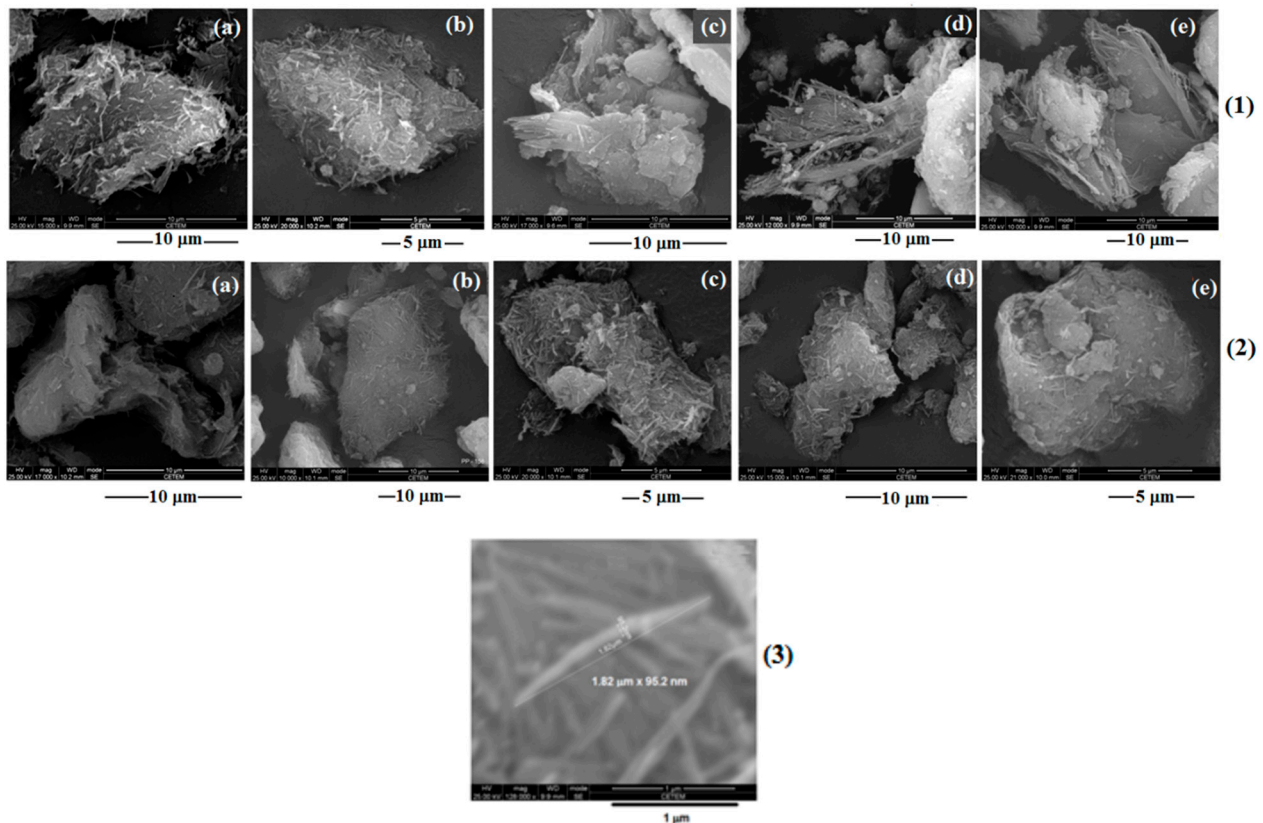


**Figure 4.** SEM images of Palys before (1) and after  $Fe^{3+}$  adsorption (2): (a) Paly I; (b) Paly II; (c) Paly III; (d) Paly IV and (e) Paly V, with different magnifications in order to better observe Palys' morphologies. (3) Secondary electron image detail of Paly I.

### 3.2.3. SEM/EDS Mappings—Mg Distribution

Figure 5 presents the acquired EDS spectra (Figure 5(1a)–(5a)) with the corresponding BSE images (Figure 5(1b)–(5b)), as well the X-ray maps showing the distribution of Mg in Paly before  $\text{Fe}^{3+}$  adsorption (Figure 5(1c)–(5c)). The chemical elements observed were Si, Mg, Al, Fe, Ti and K, corroborating the findings by XRF (Table 1). Additionally, it can be seen that Mg was evenly distributed over the entire surface, revealing a uniform and homogeneous distribution of Mg on all five Paly samples' surfaces. Thus, we can assume that the adsorption of  $\text{Fe}^{3+}$  also followed the same behavior and occurred uniformly on all Paly surfaces.

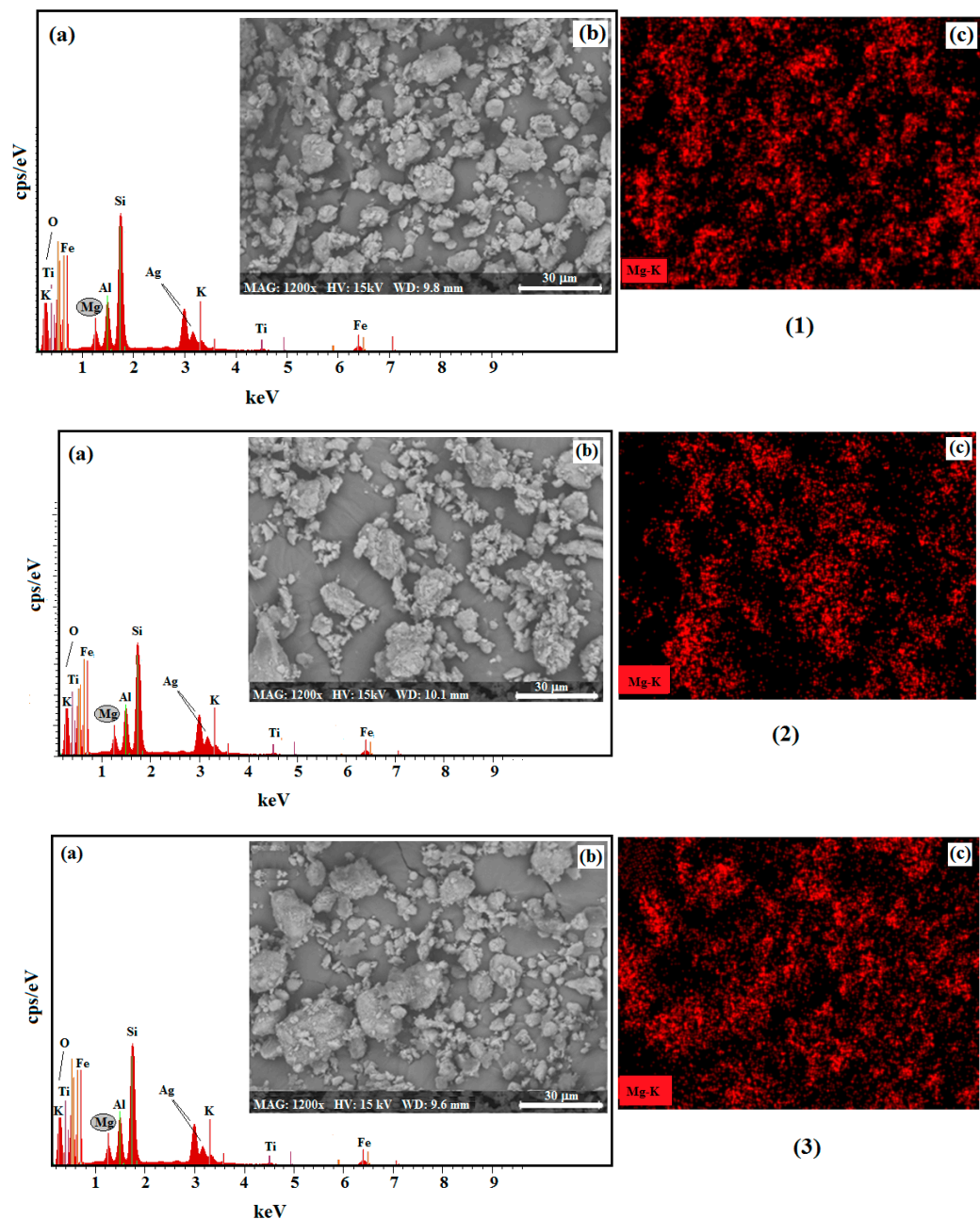
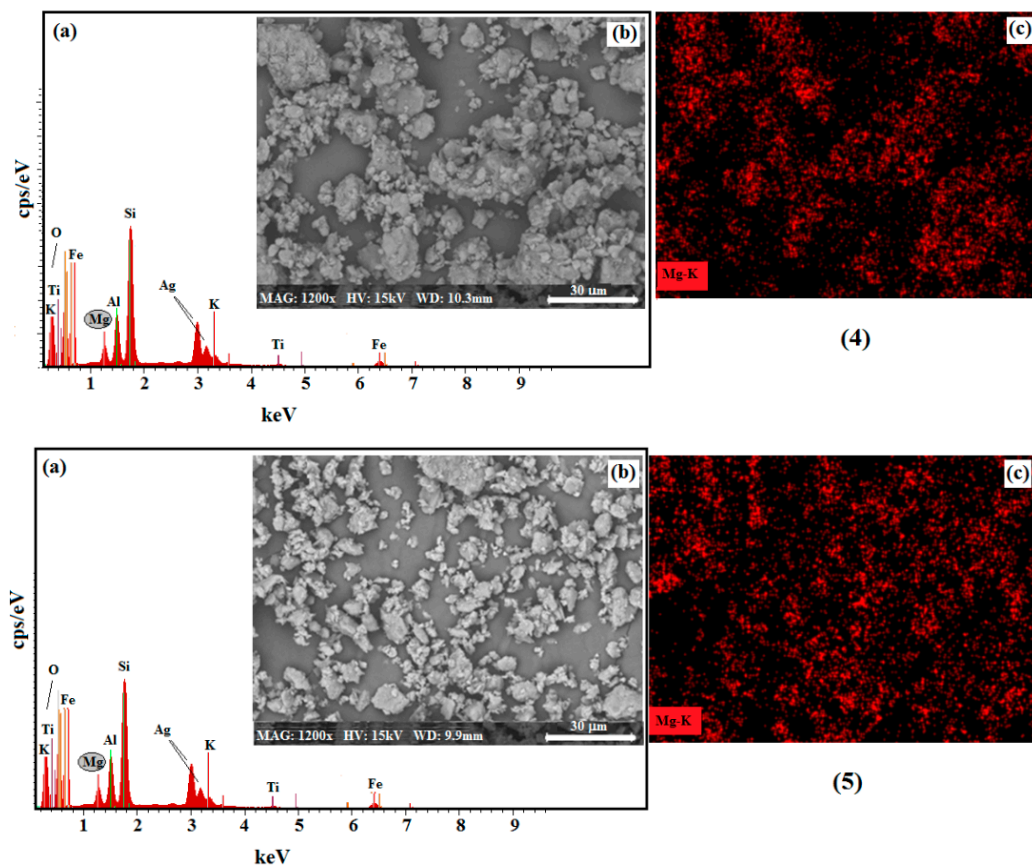


Figure 5. Cont.



**Figure 5.** (a) Acquired EDS spectra; (b) corresponding BSE images and (c) X-ray maps showing the distribution of Mg (in red) in Paly before Fe<sup>3+</sup> adsorption: (1) Paly I; (2) Paly II; (3) Paly III; (4) Paly IV and (5) Paly V.

The results of the semi-quantitative chemical analyses of Paly and Paly-Fe<sup>3+</sup> are summarized in Table 2. For this purpose, the average of three measurements was calculated in three different areas of the samples and normalized to 100%.

**Table 2.** Semi-quantitative SEM/EDS (wt%) analyses of Paly before and after Fe<sup>3+</sup> adsorption.

Elements (%)	Paly I		Paly II		Paly III		Paly IV		Paly V	
	Before	After	Before	After	Before	After	Before	After	Before	After
O	43.6	50.7	40.9	47.8	45.2	46.5	39.5	49.0	40.7	49.9
Si	30.1	22.4	31.6	22.9	26.9	24.7	31.9	24.4	30.2	21.9
Mg	3.9	2.0	3.6	2.4	4.0	2.3	3.6	1.7	2.5	2.5
Al	9.1	6.9	10.6	7.3	10.2	7.3	12.4	6.7	12.1	6.5
Fe	8.4	14.3	7.1	15.2	7.2	14.8	7.1	13.3	8.5	14.2
Ti	0.7	0.5	0.8	1.2	1.3	1.1	1.0	0.6	0.7	0.9
K	4.2	3.2	5.4	3.2	5.2	3.3	4.5	4.3	5.3	4.1
Total	100	100	100	100	100	100	100	100	100	100

Highlighted: MgO represents principal palygorskite content and Fe<sub>2</sub>O<sub>3</sub> shows the increase in iron content after adsorption.

As can be seen, Mg presented a value of around 3% before  $\text{Fe}^{3+}$  adsorption, whereas Paly III had a slightly higher value of around 4% Mg. In relation to Fe, there was an increase of approximately twice the initial value.

The EDS chemical analyses of Palys and Palys- $\text{Fe}^{3+}$  confirmed the previous results obtained by XRF (Table 1) and XRD (Figure 3), suggesting that the Paly samples had very similar characteristics.

### 3.2.4. Particle Size Distribution

Figure 6 presents the size distribution of the Palys and Palys- $\text{Fe}^{3+}$  using laser diffraction with a Malvern Mastersizer 2000 (see Figure 6a) and dynamic light scattering with a Zetasizer Nano ZS (Figure 6b), respectively. The Palys and Palys- $\text{Fe}^{3+}$  presented similar behavior, where no size distribution variation was observed by the two techniques employed, around 2.0  $\mu\text{m}$  with the Masterzizer and 0.4  $\mu\text{m}$  with the Nanosizer, showing no increase in size distribution after adsorption along with nanometer sizes, as expected. Additionally, Paly and Paly- $\text{Fe}^{3+}$  density measurements by He pycnometry are shown in Figure 6c, where it can also be seen that no important changes occurred in their densities, which remained around 2.5  $\text{g}/\text{cm}^3$ .

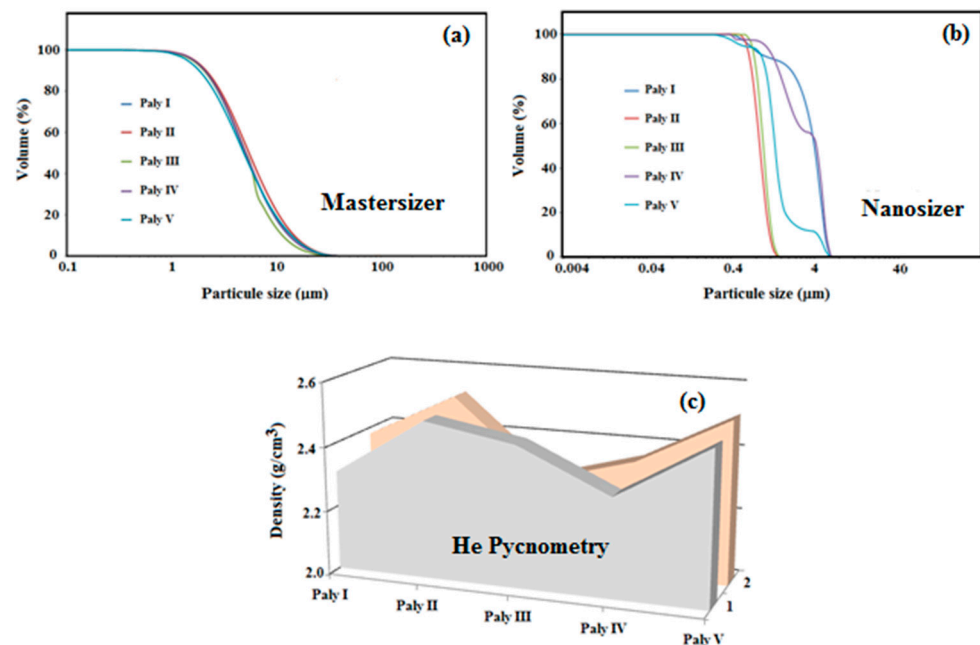


**Figure 6.** Cumulative oversize of the Palys' size distributions before and after  $\text{Fe}^{3+}$  adsorption using (a) Mastersizer; (b) Nanosizer and (c) nanoparticle density measurements for (1) Palys and (2) Palys- $\text{Fe}^{3+}$ .

### 3.2.5. SQUID—Magnetic Properties

The magnetic properties measured by the SQUID method as a function of applied magnetic field strength of 4 K, 50 K, 100 K and 200 K for Paly samples are shown in Figure 7. The results indicate typical behavior of non-magnetic materials [33,51,52] since the samples showed low magnetization saturation despite the low temperatures. The maximum observed magnetization was about 0.0004  $\text{Am}^2/\text{kg}$  for magnetic fields of 5 Tesla and temperature of 4 K. This non-magnetic behavior suggests the possibility that the  $\text{Fe}_2\text{O}_3$  concentration results presented by XRF (Table 1) refer to clinocllore impurity  $[\text{Fe}_6\text{Si}_4\text{O}_{10}(\text{OH})_8]$ , shown in Figure 3.

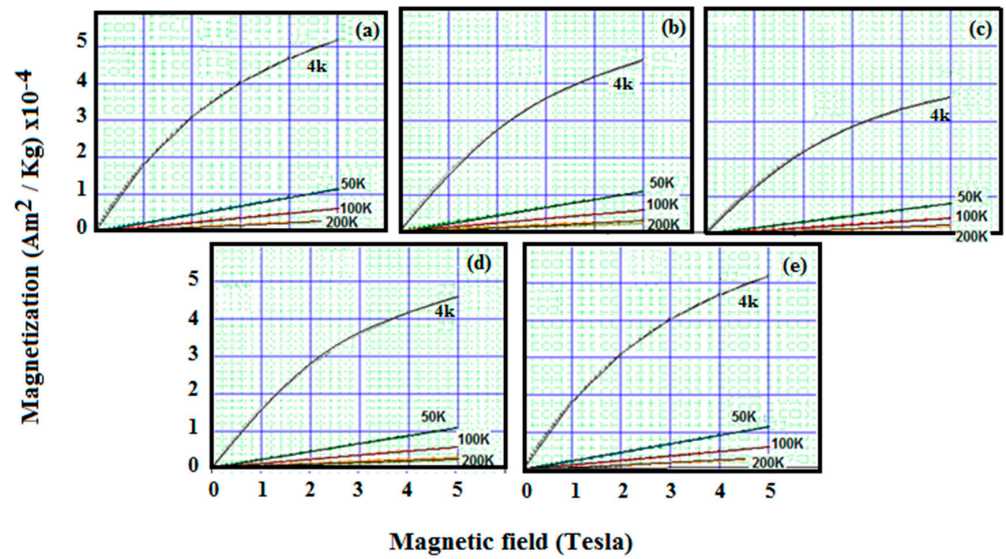


Figure 7. Magnetization curves of Palys at 4 K, 50 K, 100 K and 200 K: (a) Paly I; (b) Paly II; (c) Paly III; (d) Paly IV and (e) Paly V.

3.2.6. FTIR Analysis

Figure 8 shows the FTIR spectra of Palys and Palys-Fe<sup>3+</sup>. As can be seen from Figure 8(1), the absorption bands at 3700 cm<sup>-1</sup> may be related to the stretching vibration of the Mg-OH group present in the samples. Likewise, characteristic absorption bands of Palys at 3620 cm<sup>-1</sup> and 3546 cm<sup>-1</sup> (hydroxyl vibration of water on the surface of palygorskite or in tunnels and channels) were found [9,53–56].

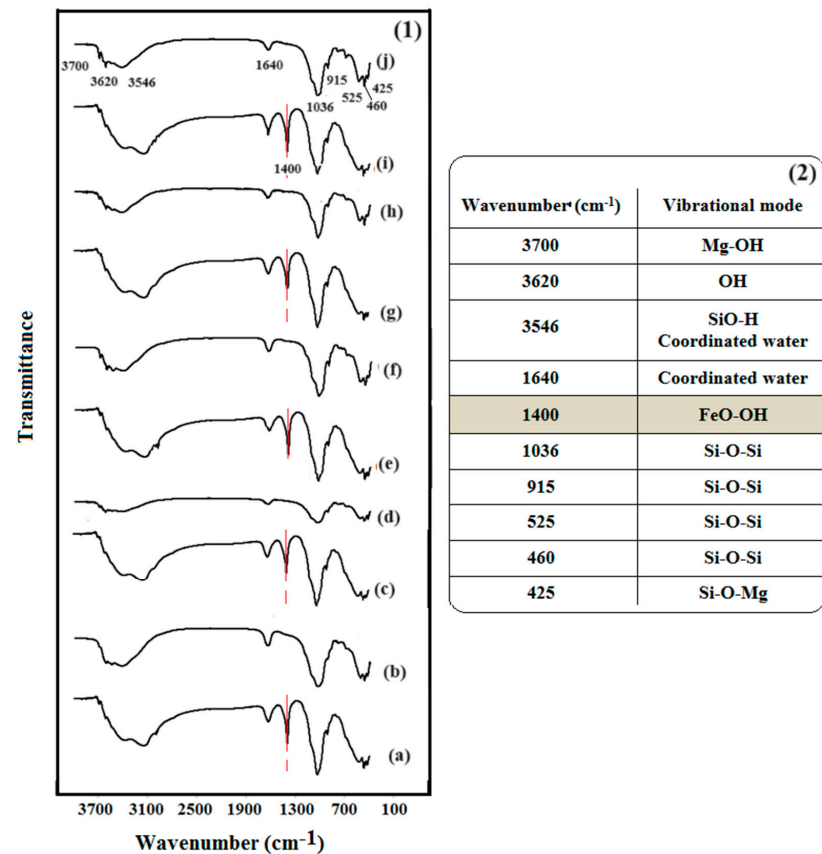


Figure 8. FTIR spectra of Palys (1) before (a,c,e,g,i) and after (b,d,f,h,j) adsorption of Fe<sup>3+</sup>: (a,b) Paly I; (c,d) Paly II; (e,f) Paly III; (g,h) Paly IV and (i,j) Paly V. (2) Summary of vibrational modes.

The band at  $1640\text{ cm}^{-1}$  can be attributed to the vibration band of coordinated water and adsorbed water molecules. In addition, the characteristic bands of Si-O-Si observed around  $1036\text{ cm}^{-1}$  and the peaks at  $915\text{ cm}^{-1}$ ,  $525\text{ cm}^{-1}$  and  $460\text{ cm}^{-1}$  can also be attributed to Si-Si bonds [55,57–60]. Finally, the bands at  $425\text{ cm}^{-1}$  can correspond to vibration of the Si-O-Mg band [61,62].

Additionally, the FTIR spectra of Palys-Fe<sup>3+</sup> presented bands at  $1400\text{ cm}^{-1}$ , related to FeO-OH stretching vibration, indicating the presence of iron oxide. This confirmed that the Paly samples' surfaces were successfully modified after Fe<sup>3+</sup> adsorption [9,59].

### 3.2.7. Thermal Stability

Three similar weight-loss steps were observed according to the TGA/DTA results for the five Palys and Palys-Fe<sup>3+</sup>, as shown in Figure 9 and summarized in Table 3. The first event was related to the evaporation of water physically adsorbed on the surface [63–65] of the Palys and Palys-Fe<sup>3+</sup> and occurred at about  $35.2\text{--}69.1\text{ }^{\circ}\text{C}$  for Palys and  $56.3\text{--}83.4\text{ }^{\circ}\text{C}$  for Palys-Fe<sup>3+</sup>, with mass losses of  $5.3\text{--}9.7\%$  and  $8.3\text{--}13.2\%$ , respectively. The second event, around  $189.3\text{--}191.9\text{ }^{\circ}\text{C}$  (Palys) and  $221.3\text{--}246.5\text{ }^{\circ}\text{C}$  (Palys-Fe<sup>3+</sup>), presented mass losses of  $2.3\text{--}2.8\%$  and  $5.8\text{--}8.2\%$  for Palys and Palys-Fe<sup>3+</sup>, respectively, related to the loss of zeolitic water molecules located in the Paly channels [9,66]. The third event, observed between  $454.2$  and  $475.4\text{ }^{\circ}\text{C}$  for Palys and  $478.9$  and  $495.7\text{ }^{\circ}\text{C}$  for Palys-Fe<sup>3+</sup>, was attributed to coordinated water loss and condensation of silanol and aluminol groups, which resulted in mass losses of  $3.6\text{--}7.5\%$  (Palys) and  $2.3\text{--}2.8\%$  (Palys-Fe<sup>3+</sup>) [67,68]. Finally, Table 3 also shows that the total mass-loss ratios were around  $14.6\text{--}16.4\%$  and  $18.8\text{--}23.4\%$  for Palys and Palys-Fe<sup>3+</sup>, respectively.

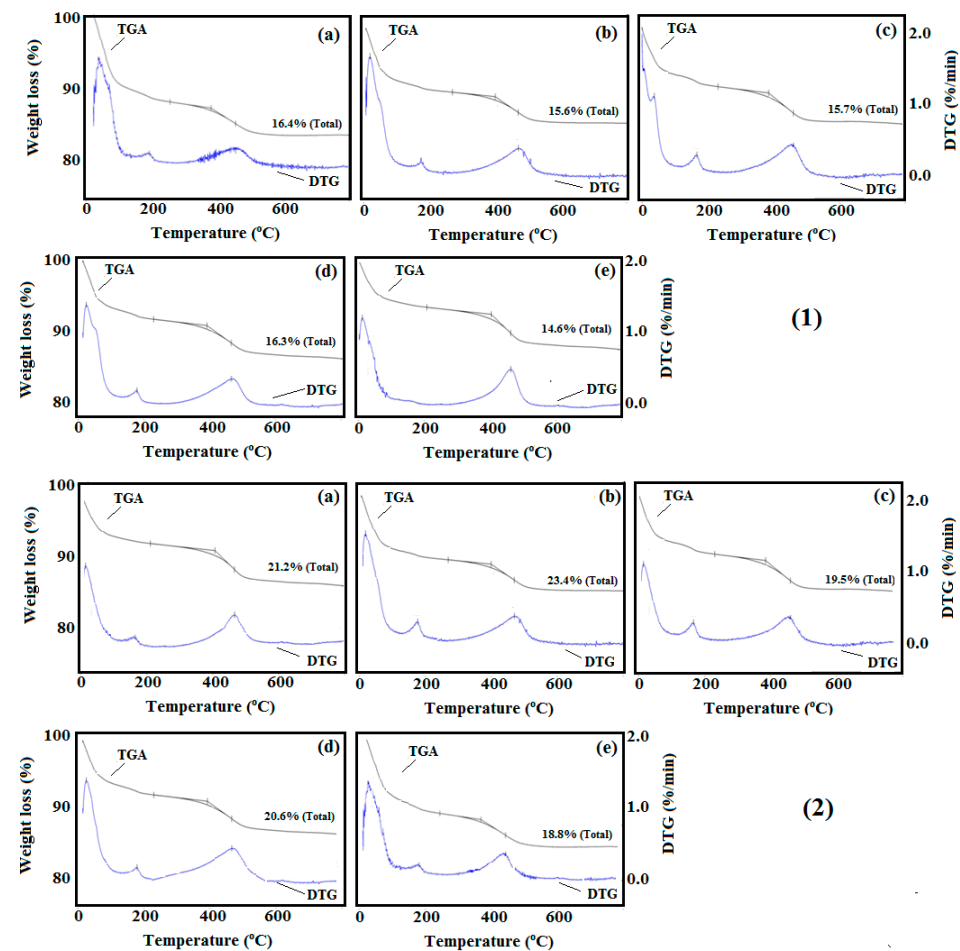


**Figure 9.** TGA weight loss and corresponding (1) DTG curves of Palys and (2) Palys-Fe<sup>3+</sup>: (a) Paly I; (b) Paly II; (c) Paly III; (d) Paly IV and (e) Paly V.

**Table 3.** TGA/DTA analysis of Palys and Palys-Fe<sup>3+</sup>.

Palys	Event 1 (°C)/Mass Loss (%)		Event 2 (°C)/Mass Loss (%)		Event 3 (°C)/Mass Loss (%)		Total Mass Loss (%)	
	Paly	Paly-Fe <sup>3+</sup>	Paly	Paly-Fe <sup>3+</sup>	Paly	Paly-Fe <sup>3+</sup>	Paly	Paly-Fe <sup>3+</sup>
Paly I	37.6/9.7	83.4/12.6	191.9/2.3	246.5/5.8	454.2/4.4	495.7/2.8	16.4	21.2
Paly II	35.2/5.3	74.8/13.2	190.7/2.8	237.9/7.4	467.6/7.5	487.1/2.8	15.6	23.4
Paly III	69.1/9.6	72.4/11.1	189.3/2.5	221.3/6.1	472.4/3.6	478.9/2.3	15.7	19.5
Paly IV	42.6/6.2	56.3/10.8	190.2/2.7	229.7/7.1	466.3/7.4	480.7/2.7	16.3	20.6
Paly V	41.3/6.8	77.1/8.3	190.5/2.3	238.4/8.2	475.4/5.5	482.9/2.3	14.6	18.8

### 3.2.8. Surface Charge—Hydrophobicity

The variations of the zeta potential of Palys and Palys-Fe<sup>3+</sup> with changes in pH are shown in Figure 10(1) and (2), respectively. In the pH range of 1–12, the values of Paly zeta potential increased with the increase in pH, since concentrations of hydroxide ions in the solution also increased and the mineral surface adsorbed a large number of free ions with negative charge, as expected [9,69,70]. The maximum value reached was −25 mV at pH 9.0, and it remained stable in the suspension system with higher pH values. This behavior favors good adsorption on cationic compounds. On the other hand, Palys-Fe<sup>3+</sup> showed a change in its charges at around pH 8.0 due to the positive charge of the Fe<sup>3+</sup> adsorbed on the Paly surfaces, which becomes positive below this pH value and negative above it, evidencing the change in Paly surfaces after Fe<sup>3+</sup> adsorption. Additionally, Figure 10(3) shows the results of the contact angle measurements for Palys and Palys-Fe<sup>3+</sup>, providing important data on the wettability of the samples before and after Fe<sup>3+</sup> adsorption. The sessile drop method was used to evaluate the hydrophobicity of pressed surfaces, as in a previous study [64]. The contact angles for all samples were zero, referring to hydrophilic surfaces with high wettability by water. This behavior is expected for silicon oxides [71].

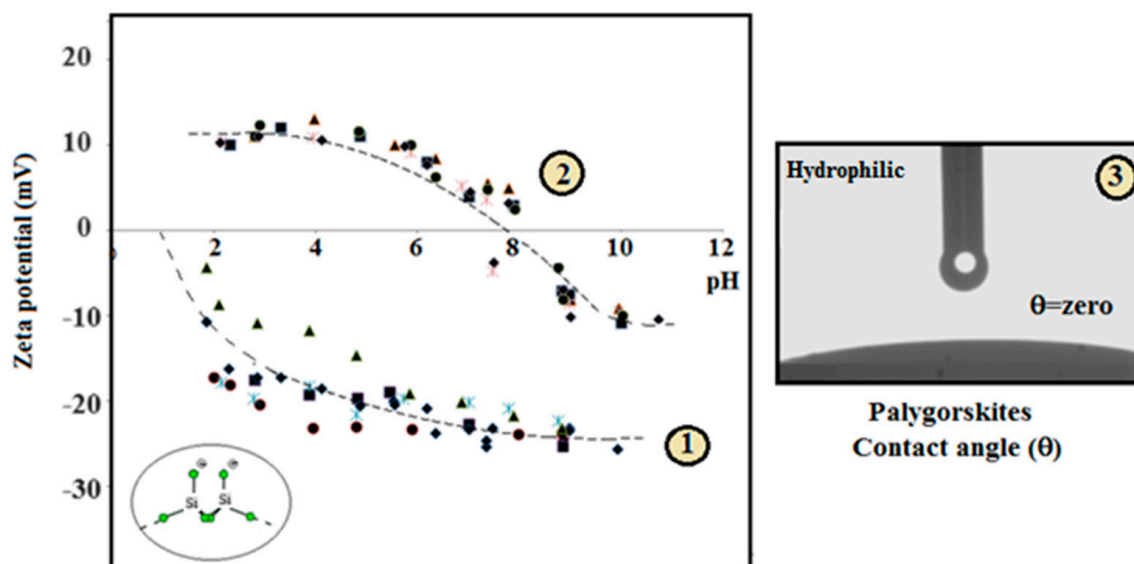


**Figure 10.** Zeta potential of Paly nanoparticles (1) before and (2) after Fe<sup>3+</sup> adsorption: (●) Paly I; (■) Paly II; (▲) Paly III; (◆) Paly IV and (✱) Paly V. (3) Paly contact angle (θ) before and after Fe<sup>3+</sup> adsorption.

### 3.3. Adsorption Studies: Evaluation of Fe<sup>3+</sup> Adsorption on Five Paly Surfaces

#### 3.3.1. Adsorption Kinetics

The adsorption kinetics of the five Palys studied in this work is shown in Figure 11. The effect of contact time of Fe<sup>3+</sup> onto Palys surfaces was investigated at various time intervals in the range 0–6 h (Figure 11(1)). As can be seen, the Fe<sup>3+</sup> adsorption capacity

increased very rapidly in the first 30 min and reached around 44 mg/g (the maximum Fe<sup>3+</sup> equilibrium adsorption capacity) at 1 h then remained constant. This behavior was similar for all Pals, mainly due to the active sites on the Paly surfaces that were available at the beginning of the adsorption process. For the adsorption isotherm studies, a contact time of three hours was used to ensure complete adsorption.

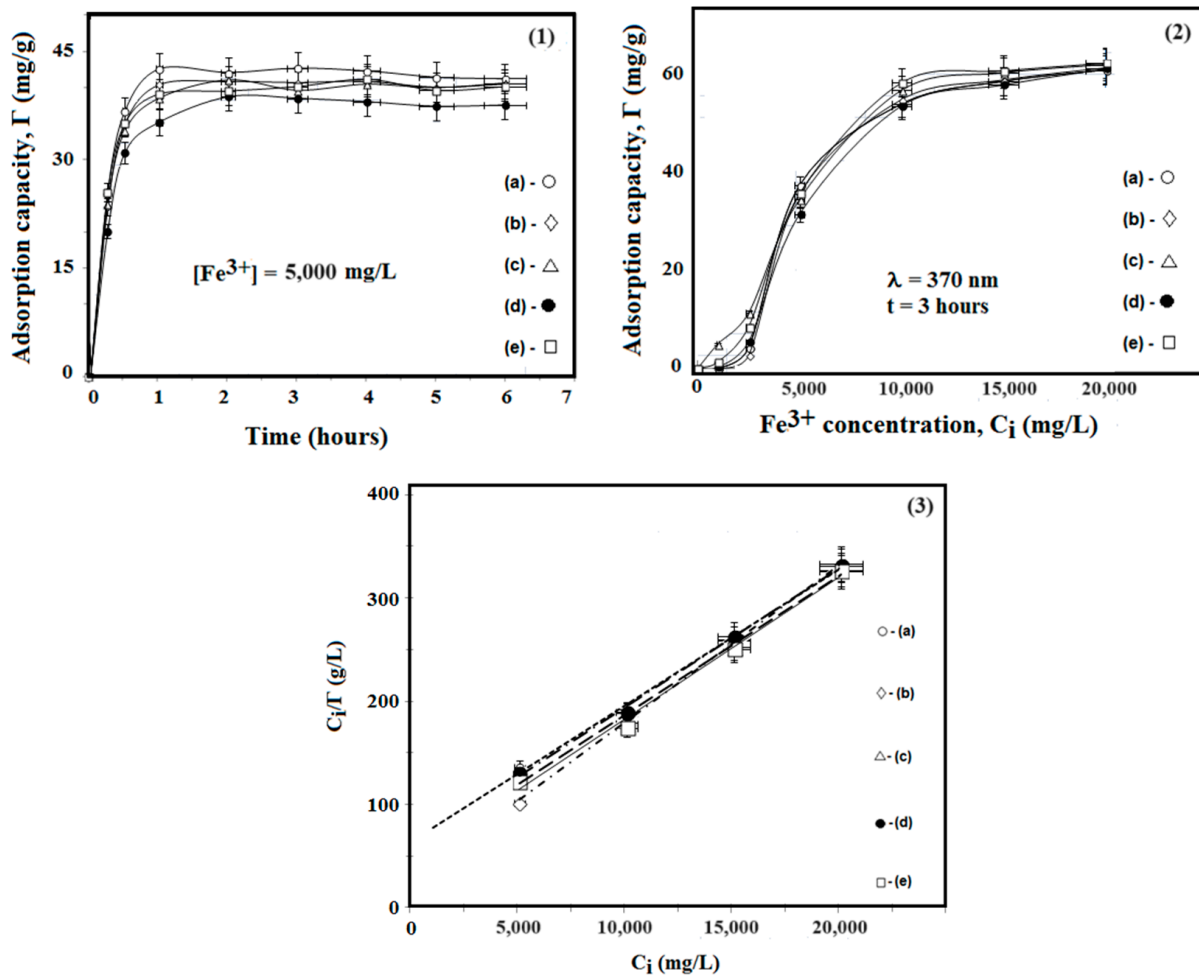


**Figure 11.** Adsorption studies: (1) influence of mixing time on the adsorption of Fe<sup>3+</sup> by Pals; (2) Fe<sup>3+</sup> adsorption capacity isotherms and their goodness of fit to the theoretical Langmuir equation; (3) Langmuir plot for the adsorption of Fe<sup>3+</sup> onto Pals.

### 3.3.2. Adsorption Isotherm

The equilibrium adsorption capacity of Fe<sup>3+</sup> onto Pals and the corresponding adsorption isotherms are plotted in Figure 11(2). It is clear that the adsorption capacity of the Fe<sup>3+</sup> onto Pals increased with an increase in the Fe<sup>3+</sup> concentration in solution and reached saturation gradually.

The maximum equilibrium adsorption capacity of around 60 mg/g was observed at an initial Fe<sup>3+</sup> concentration of 10,000 mg/L. According to the classification of Giles et al. [72], the isotherm was supposedly of the Langmuir type, indicating that the Fe<sup>3+</sup> has a high affinity for the Paly surfaces.

The Langmuir adsorption isotherm assumes that adsorption occurs at specific homogeneous sites within the adsorbent, and it has been successfully applied in many studies of monolayer adsorption. The linear form of the Langmuir isotherm equation is written as:

$$C_i/\Gamma = 1/K \cdot \Gamma_m + 1/\Gamma_m \cdot C_i \quad (2)$$

where  $\Gamma$  is the equilibrium capacity of  $\text{Fe}^{3+}$  on the adsorbent (mg/g),  $C_i$  is the initial concentration of the  $\text{Fe}^{3+}$  solution (mg/L),  $\Gamma_m$  is the monolayer adsorption capacity of the adsorbent (mg/g) and  $k$  is the Langmuir adsorption constant (L/mg), related to the free energy of adsorption.

The adsorption equation was obtained from experimental data (Equation (2)). The isotherm constants and correlation coefficients were calculated from the linear Langmuir plots by plotting  $C_i/\Gamma$  vs.  $C_i$  (see Figure 11(3)) and are presented in Table 4. The Langmuir equation represented the adsorption process very well, as can be seen by the  $R^2$  values. This may have been due to the homogeneous distribution of active sites on the palygorskite surface, as reported by some authors who have stated that the adsorption of  $\text{Fe}^{3+}$  on palygorskite is supposedly described by the Langmuir equation [9,64,73,74]. This result indicates that the studied Palys possess a very high adsorption capacity, so the mineral is very useful in removing  $\text{Fe}^{3+}$  from aqueous solutions.

**Table 4.** Adsorption thermodynamic parameters.

Palys Sample	$R^2$	$1/K\Gamma_m$ (g/L)	$1/\Gamma_m$ (mg/g)	$K$ (L/mol)	$\Delta G$ (KJ/mol)
Paly I	0.9939	44.500	0.0138	50.39	−9.71
Paly II	0.9935	52.000	0.0135	42.19	−9.27
Paly III	0.9986	27.345	0.0152	90.33	−11.16
Paly IV	0.9980	59.050	0.0135	37.15	−8.96
Paly V	0.9943	62.745	0.0132	34.19	−8.75

Highlighted: Paly III showed more conducive to  $\text{Fe}^{3+}$  adsorption.

The values of  $\Delta G$  for Palys were all negative and close to each other. The negative  $\Delta G$  values indicate that the process of  $\text{Fe}^{3+}$  adsorption was spontaneous. The absolute value of  $\Delta G$  was highest for Paly III (11.16 KJ/mol), indicating that this sample was more conducive to  $\text{Fe}^{3+}$  adsorption.

### 3.4. Additional Characterizations of Paly III (BET Surface Area Analysis/AFM)

The five Palys studied had very similar characteristics, so we chose the Paly III sample, which had the highest negative  $\Delta G$  value, for evaluation in relation to its porosity by BET and AFM. It will certainly represent the others.

#### BET—AFM

The specific surface areas and porous parameters of Paly III alone and with  $\text{Fe}^{3+}$  adsorbed (Paly III- $\text{Fe}^{3+}$ ) are shown in Tables 5–7 and Figure 12. The nitrogen adsorption–desorption isotherms of the Paly III and Paly III- $\text{Fe}^{3+}$  (see Figure 12a,b) were classified as typical type II isotherms that yield nonporous or macroporous adsorbents according to the IUPAC classification [75]. The hysteresis loops of Paly III and Paly III- $\text{Fe}^{3+}$  were similar, indicating that the adsorption of  $\text{Fe}^{3+}$  onto Paly III did not change the former's porous structure. The amount of  $\text{N}_2$  adsorbed gradually increased with rising relative pressure, and the adsorption and desorption lines completely overlap each other, suggesting a monolayer adsorption [45]. The BET specific surface area of 108.9  $\text{m}^2/\text{g}$  for Paly III decreased to 102.4  $\text{m}^2/\text{g}$  for Paly III- $\text{Fe}^{3+}$  (Table 5 and Figure 12c), which might be due to the increase of steric hindrance leading to a smaller Paly III- $\text{Fe}^{3+}$  surface area. The average pore diameters from the BJH pore-size distribution pattern were 94.84 Å and 77.08 Å, respectively, indicating nonporous or macroporous adsorbents (Table 7). The external surface areas and micropore volumes (Tables 5 and 6) were calculated by using the t-plot method. For Paly III, a micropore volume of 0.01097  $\text{cm}^3/\text{g}$  was measured, with a micropore area of 25.89  $\text{m}^2/\text{g}$  and a larger external surface area of 82.98  $\text{m}^2/\text{g}$ . For Paly III- $\text{Fe}^{3+}$ , the micropore volume and micropore area values decreased to 0.002416  $\text{cm}^3/\text{g}$  and 7.42  $\text{m}^2/\text{g}$ , respectively, which can be explained by the decrease of ordered degree of the macroporous structure due to  $\text{Fe}^{3+}$  adsorbed onto Paly III.

**Table 5.** Surface area (m<sup>2</sup>/g).

Paly	BET Single Point <sup>a</sup>	BET	Langmuir	t-Plot Micropore	t-Plot External	BJH Adsorption <sup>b</sup>	BJH Desorption <sup>b</sup>
Paly III	106.65	108.87	148.79	25.89	82.98	91.27	102.41
Paly III-Fe <sup>3+</sup>	98.74	102.40	141.64	7.42	94.98	117.15	117.51

<sup>a</sup>  $p/p_0 = 0.199$ . <sup>b</sup> BJH (adsorption and desorption) cumulative surface area of pores between 17.000 Å and 3000.000 Å width.

**Table 6.** Pore volume (cm<sup>3</sup>/g).

Paly	Single Point Adsorption	Single Point Desorption	t-Plot Micropore	BJH Adsorption <sup>c</sup>	BJH Desorption <sup>c</sup>
Paly III	0.2098 <sup>a</sup>	0.2187 <sup>b</sup>	0.01097	0.2164	0.2212
Paly III-Fe <sup>3+</sup>	0.2163 <sup>d</sup>	0.2181 <sup>e</sup>	0.002416	0.2257	0.2068

<sup>a</sup> Total pore volume of pores less than 867.838 Å width at  $p/p_0 = 0.9771$ . <sup>b</sup> Total pore volume of pores less than 699.660 Å width at  $p/p_0 = 0.9715$ . <sup>c</sup> BJH (adsorption and desorption) cumulative volume of pores between 17.000 Å and 3000.000 Å width. <sup>d</sup> Total pore volume of pores less than 1098.150 Å width at  $p/p_0 = 0.9820$ . <sup>e</sup> Total pore volume of pores less than 713.725 Å width at  $p/p_0 = 0.9721$ .

**Table 7.** Pore size (Å).

Paly	Adsorption <sup>a</sup>	Desorption <sup>a</sup>	BJH Adsorption <sup>b</sup>	BJH Desorption <sup>b</sup>
Paly III	77.09	80.34	94.84	86.42
Paly III-Fe <sup>3+</sup>	84.51	85.18	77.08	70.40

<sup>a</sup> Average pore width (4 V/A by BET). <sup>b</sup> Average pore width (4 V/A).

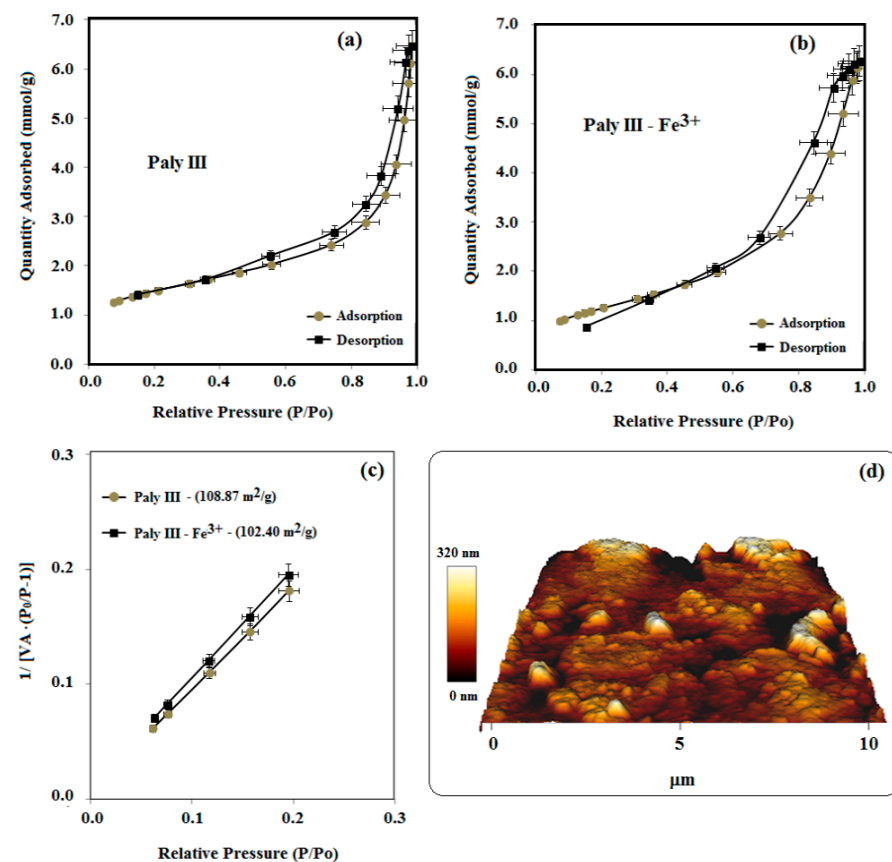


**Figure 12.** (a) Nitrogen adsorption–desorption isotherm for Paly III; (b) nitrogen adsorption–desorption isotherm for Paly III-Fe<sup>3+</sup>; (c) specific surface areas for Paly III and Paly III-Fe<sup>3+</sup> and (d) three-dimensional AFM topographic image of Paly III crystals.

As observed from Figure 12, the major contribution to specific surface area of the samples came from the external surface. The surface area decreased with the  $\text{Fe}^{3+}$  adsorption on Paly III, and the pores had width between 70–95 Å (Table 7). Thus, it can be stated that having a porous structure and large specific surface areas is very favorable for the adsorption and removal of  $\text{Fe}^{3+}$  from water.

This behavior was confirmed by observing Paly III's high-resolution AFM image, showing its texture (Figure 12d) and spherical particles with different mean sizes in the range of 0–10  $\mu\text{m}$ . Various grain sizes distributed over the entire surface of Paly III can be observed. These grains are formed by smaller grains with a diameter of approximately 150 nm. The maximum height of the largest cluster of grains was approximately 320 nm, with RMS roughness of approximately 74 nm. Furthermore, a variety of colors is present, indicating that the Paly sample has other components, as observed by the characterization by XRF, XRD, FTIR and EDS.

#### 4. Conclusions

The removal of  $\text{Fe}^{3+}$  ions from aqueous solutions by adsorption on five natural eco-friendly Brazilian palygorskites for environmental applications was investigated and characterized by various analyses after quartz-reduced efficiency of around 80% was shown by XRD.

The five Paly samples presented very similar characteristics, probably due to the proximity of the geological formation and the extraction location. The impurities found by XRF and XRD were clinocllore, kaolinite, quartz, anatase and diaspore, while  $\text{SiO}_2$  was the main component found, around 50% (*w/w*), due to the presence in the composition of palygorskite and quartz minerals. The Paly had a fibrous aspect according to SEM observation and formed aggregates, typical behavior of nanometric particles, as confirmed by the particle size distribution techniques. In general, the characterization methods used in this work indicated that the samples had typical characteristics of palygorskite minerals, such as no magnetism, negative charge and hydrophilicity.

Paly surface modification after  $\text{Fe}^{3+}$  adsorption was evidenced by the increase in iron concentration observed by XRF and EDS, by the appearance of the band at  $1400\text{ cm}^{-1}$  in the FTIR spectrum and by the charge change from negative to positive around pH 8.0 in the zeta potential curve.

Regarding the adsorption studies, we observed that the  $\text{Fe}^{3+}$  adsorption capacity on Paly increased very rapidly in the first 30 min, reaching a maximum  $\text{Fe}^{3+}$  equilibrium adsorption capacity of around 44 mg/g at 1 h, after which it remained constant. The maximum equilibrium adsorption capacity, around 60 mg/g, was observed at an initial  $\text{Fe}^{3+}$  concentration of 10,000 mg/L. The Langmuir model supposedly represented the adsorption process, indicating that the  $\text{Fe}^{3+}$  has high affinity for the Paly surfaces.

Finally, the values of  $\Delta G$  for Paly were all negative, meaning that the process of  $\text{Fe}^{3+}$  adsorption was spontaneous and very promising for the removal of  $\text{Fe}^{3+}$  from wastewater.

**Author Contributions:** Conceptualization: L.d.S.S., R.N., F.G.d.S.J. and O.d.F.M.G.; Methodology: A.M., T.d.L.A.P.F., L.C.d.L. and V.M.T.S.B.; Validation: A.M., L.d.S.S., R.N., F.G.d.S.J. and O.d.F.M.G.; Formal Analysis: A.M., T.d.L.A.P.F., L.C.d.L. and V.M.T.S.B.; Investigation: A.M., R.N. and F.G.d.S.J. Writing—Original Draft Preparation: A.M.; Supervision: L.d.S.S., R.N., F.G.d.S.J. and O.d.F.M.G.; Project Administration: R.N. and L.d.S.S. All authors have read and agreed to the published version of the manuscript.

**Funding:** This research received no external funding.

**Data Availability Statement:** The data presented in this study are openly available in article.

**Acknowledgments:** The authors acknowledge the support of the Center for Mineral Technology (CETEM), Federal University of Rio de Janeiro/Institute of Macromolecules (UFRJ/IMA), Federal University of Rio de Janeiro/COPPE Nanotechnology Engineering Program (UFRJ/COPPE) and Federal University of Rio de Janeiro/Physics Institute UFRJ/IF, along with Colorminas Colorífico e Mineração for supplying the palygorskite samples.

**Conflicts of Interest:** The authors declare no conflicts of interest.

## References

1. Ostroski, I.C.; Barros, M.A.S.D.; Silva, E.A.; Dantas, J.H.; Arroyo, P.A.; Lima, C.O.M. The Removal of Fe (III) Ions by Adsorption onto Zeolite Columns. *Adsorpt. Sci. Technol.* **2007**, *25*, 757–768. [CrossRef]
2. Aksu, Z. Application of biosorption for the removal of organic pollutants: A review. *Process Biochem.* **2005**, *40*, 997–1026. [CrossRef]
3. Sheibani, A.; Shishehbor, M.R.; Alaei, H. Removal of Fe (III) ions from aqueous solution by hazelnut hull as an adsorbent. *Int. J. Ind. Chem.* **2012**, *3*, 4. [CrossRef]
4. Liang, X.; Xu, Y.; Tan, X.; Wang, L.; Sun, Y.; Lin, D.; Sun, Y.; Qin, X.; Wang, Q. Heavy metal adsorbents mercapto and amino functionalized palygorskite: Preparation and characterization. *Colloids Surfaces A Physicochem. Eng. Asp.* **2013**, *426*, 98–105. [CrossRef]
5. Shaheen, S.M.; Eissa, F.I.; Ghanem, K.M.; El-Din, H.M.G.; Al Anamy, F.S. Heavy metals removal from aqueous solutions and wastewaters by using various byproducts. *J. Environ. Manag.* **2013**, *128*, 514–521. [CrossRef] [PubMed]
6. Qian, G.; Li, M.; Wang, F.; Liu, X. Removal of Fe<sup>3+</sup> from Aqueous Solution by Natural Apatite. *J. Surf. Eng. Mater. Adv. Technol.* **2014**, *4*, 14–20. [CrossRef]
7. Zhu, Y.; Chen, T.; Liu, H.; Xu, B.; Xie, J. Kinetics and thermodynamics of Eu (III) and U (VI) adsorption onto palygorskite. *J. Mol. Liq.* **2016**, *219*, 272–278. [CrossRef]
8. Al-Anber, Z.A.; Al-Anber, M.A.S. Thermodynamics and Kinetic Studies of Iron (III) Adsorption by Olive Cake in a Batch System. *J. Mex. Chem. Soc.* **2008**, *52*, 108–115. Available online: <https://www.jmcs.org.mx/index.php/jmcs/article/view/1055/867> (accessed on 14 July 2022).
9. Middea, A.; Fernandes, T.L.A.P.; Neumann, R.; Gomes, O.F.M.; Spinelli, L.S. Evaluation of Fe (III) adsorption onto palygorskite surfaces. *Appl. Surf. Sci.* **2013**, *282*, 253–258. [CrossRef]
10. Perlatti, F.; Ruiz, F.; Otero, X.L.; Ferreira, T.O. Adsorption and Sequential Extraction of Copper in Technosols Prepared from Unconsolidated Mining Wastes Rich in Limestone, Bentonite, and Organic Matter. *Mining* **2023**, *3*, 151–162. [CrossRef]
11. Hassanin, M.A.; Negm, S.H.; Youssef, M.A.; Sakr, A.K.; Mira, H.I.; Mohammaden, T.F.; Al-Otaibi, J.S.; Hanfi, M.Y.; Sayyed, M.I.; Cheira, M.F. Sustainable Remedy Waste to Generate SiO<sub>2</sub> Functionalized on Graphene Oxide for Removal of U(VI) Ions. *Sustainability* **2022**, *14*, 2699. [CrossRef]
12. Xuan, G.X.; Zhang, G.H.; Cheng, W.C.; Ma, C.Y.; Li, Q.R.; Liu, E.T.; He, W.G.; Dong, F.Q.; Li, X.A.; Chen, Z.G.; et al. Uranium Speciation and Distribution on the Surface of *Shewanella Putrefaciens* in the Presence of Inorganic Phosphate and Zero-Valent Iron under Anaerobic Conditions. *Sci. Total Environ.* **2024**, *912*, 169438. [CrossRef]
13. Murray, H.H. Traditional and new applications for kaolin, smectite and palygorskite: A general overview. *Appl. Clay Sci.* **2000**, *17*, 207–221. [CrossRef]
14. Neaman, A.; Singer, A. Possible use of the Sacalum (Yucatan) palygorskite as drilling muds. *Appl. Clay Sci.* **2004**, *25*, 121–124. [CrossRef]
15. Neaman, A.; Singer, A. The effects of palygorskite on chemical and physico-chemical properties of soils: A review. *Geoderma* **2004**, *123*, 297–303. [CrossRef]
16. Deng, Y.; Gao, Z.; Liu, B.; Hu, X.; Wei, Z.; Sun, C. Selective removal of lead from aqueous solutions by ethylenediamine-modified attapulgite. *Chem. Eng. J.* **2013**, *223*, 91–98. [CrossRef]
17. Bourliva, A.; Sikalidis, A.K.; Papadopoulou, L.; Betsiou, M.; Michailidis, K.; Sikalidis, C.; Filippidis, A. Removal of Cu<sup>2+</sup> and Ni<sup>2+</sup> ions from aqueous solutions by adsorption onto natural palygorskite and vermiculite. *Clay Miner.* **2018**, *53*, 1–15. [CrossRef]
18. Suárez, M.; García-Rivas, J.; Morales, J.; Lorenzo, A.; García-Vicente, A.; García-Romero, E. Review and new data on the surface properties of palygorskite: A comparative study. *Appl. Clay Sci.* **2022**, *216*, 106311. [CrossRef]
19. Bailey, S.W. Structures of Layer Silicates. In *Crystal Structures of Clay Minerals and their X-ray Identification*; Brindley, G.W., Brown, G., Eds.; Mineralogical Society of Great Britain and Ireland: Twickenham, UK, 1980; pp. 1–123. [CrossRef]
20. Yan, W.; Liu, D.; Tan, D.; Yuan, P.; Chen, M. FTIR spectroscopy study of the structure changes of palygorskite under heating. *Spectrochim. Acta Part A Mol. Biomol. Spectrosc.* **2012**, *97*, 1052–1057. [CrossRef]
21. Fraser, M.B.; Churchman, G.J.; Chittleborough, D.J.; Rengasamy, P. Effect of plant growth on the occurrence and stability of palygorskite, sepiolite and saponite in salt-affected soils on limestone in South Australia. *Appl. Clay Sci.* **2016**, *124–125*, 183–196. [CrossRef]
22. Oliveira, A.M.B.M.; Coelho, L.F.O.; Gomes, S.S.S.; Costa, I.F.; Fonseca, M.G.; Souza, K.S.; Espínolo, J.G.P.; Filho, E.C.S. Brazilian palygorskite as adsorbent for metal; ions from aqueous solution—Kinetic and equilibrium studies. *Water Air Soil Pollut.* **2013**, *224*, 1687. [CrossRef]
23. Oliveira, R.N.; Acchar, W.; Soares, G.D.A.; Barreto, L.S. The increase of surface area of a Brazilian palygorskite clay activated with sulfuric acid solutions using a factorial design. *Mater. Res.* **2013**, *16*, 924–928. [CrossRef]
24. Xavier, K.C.M.; Santos, M.S.F.; Osajima, J.A.; Luz, A.B.; Fonseca, M.G.; Filho, E.C.S. Thermally activated palygorskites as agents to clarify soybean oil. *Appl. Clay Sci.* **2016**, *119*, 338–347. [CrossRef]

25. Assis, T.C.; Cerqueda, M.; Souza, C.G.; Jesus, T.C.; Marçano, G.B.; Simões, K.M.A.; Rodrigues, P.V.; Furlanetto, R.P.P.; Anjos, N.O.A.; Nascimento, L.C.S.; et al. Comparative Analysis of Palygorskite Samples From Different Occurrences in Guadalupe (Piauí, Brazil). *J. Aerosol. Technol. Manag.* **2019**, *11*, 62–65. [[CrossRef](#)]
26. Souza, C.G.; Jesus, T.C.L.; Santos, R.C.; Bomfim, L.M.; Bertolino, L.C.; Andrade, D.F.; d'Avila, L.A.; Spinelli, L.S. Characterization of Brazilian palygorskite (Guadalupe region) and adsorptive behaviour for solvatochromic dyes. *Clay Miner.* **2021**, *56*, 55–64. [[CrossRef](#)]
27. Meirelles, L.M.A.; Barbosa, R.d.M.; Sanchez-Espejo, R.; García-Villén, F.; Perioli, L.; Viseras, C.; Moura, T.F.A.d.L.e.; Raffin, F.N. Investigation into Brazilian Palygorskite for Its Potential Use as Pharmaceutical Excipient: Perspectives and Applications. *Materials* **2023**, *16*, 4962. [[CrossRef](#)] [[PubMed](#)]
28. Carretero, M.I.; Pozo, M. Clay and non-clay minerals in the pharmaceutical and cosmetic industries Part II. Active ingredients. *Appl. Clay Sci.* **2010**, *47*, 171–181. [[CrossRef](#)]
29. Celik, H. Technological characterization and industrial application of two Turkish clays for the ceramic industry. *Appl. Clay Sci.* **2010**, *50*, 245–254. [[CrossRef](#)]
30. Li, W.; Adams, A.; Wang, J.; Blümich, B.; Yang, Y. Polyethylene/palygorskite nanocomposites: Preparation by in situ polymerization and their characterization. *Polymer* **2010**, *51*, 4686–4697. [[CrossRef](#)]
31. Abdo, J.; Haneef, M.D. Clay nanoparticles modified drilling fluids for drilling of deep hydrocarbon wells. *Appl. Clay Sci.* **2013**, *86*, 76–82. [[CrossRef](#)]
32. Soares, D.S.; Fernandes, C.S.; Costa, A.C.S.; Raffin, F.N.; Acchar, W.; Moura, T.F.A.L. Characterization of palygorskite clay from Piauí, Brazil and its potential use as excipient for solid dosage forms containing anti-tuberculosis drugs. *J. Therm. Anal. Calorim.* **2013**, *113*, 551–558. [[CrossRef](#)]
33. Middea, A.; Spinelli, L.S.; Souza Junior, F.G.; Neumann, R.; Gomes, O.F.M.; Fernandes, T.L.A.P.; Lima, L.C.; Barthem, V.M.T.S.; Carvalho, F.V. Synthesis and characterization of magnetic palygorskite nanoparticles and their application on methylene blue removal from water. *Appl. Surf. Sci.* **2015**, *346*, 232–239. [[CrossRef](#)]
34. Oliveira, M.E.R.; Santos, L.M.; Silva, M.L.G.; Cunha, H.N.; Filho, E.C.S.; Leite, C.M.S. Preparation and characterization of composite polyaniline/poly(vinyl alcohol)/palygorskite. *J. Therm. Anal. Calorim.* **2015**, *119*, 37–46. [[CrossRef](#)]
35. Zhongwei, L.; Pengxiang, L.; Zigong, N.; Yang, X.; Chengzhi, W.; Yunkai, L. A modified attapulgite clay for controlling infiltration of reclaimed water riverbed. *Environ. Earth Sci.* **2015**, *73*, 3887–3900. [[CrossRef](#)]
36. Morozov, I.A.; Garishin, O.K.; Shadrin, V.V.; Gerasin, V.A.; Guseva, M.A. Atomic force microscopy of structural-mechanical properties of polyethylene reinforced by silicate needle-shaped filler. *Adv. Mater. Sci. Eng.* **2016**, *2016*, 8945978. [[CrossRef](#)]
37. Eloussaief, M.; Kallel, N.; Yaacoubi, A.; Benzina, M. Mineralogical identification, spectroscopic characterization, and potential environmental use of natural clay materials on chromate removal from aqueous solutions. *Chem. Eng. J.* **2011**, *168*, 1024–1031. [[CrossRef](#)]
38. He, M.; Zhu, Y.; Yang, Y.; Han, B.; Zhang, Y. Adsorption of cobalt (II) ions from aqueous solutions by palygorskite. *Appl. Clay Sci.* **2011**, *54*, 292–296. [[CrossRef](#)]
39. Guo, N.; Wang, J.S.; Li, J.; Teng, Y.G.; Zhai, Y.Z. Dynamic adsorption of Cd<sup>2+</sup> onto acid-modified attapulgite from aqueous solution. *Clays Clay Miner.* **2014**, *62*, 415–424. [[CrossRef](#)]
40. Zhang, Z.; Wang, W.; Wang, A. Effects of solvothermal process on the physicochemical and adsorption characteristics of palygorskite. *Appl. Clay Sci.* **2015**, *107*, 230–237. [[CrossRef](#)]
41. Post, J.L.; Crawford, S. Varied forms of palygorskite and sepiolite from different geologic systems. *Appl. Clay Sci.* **2007**, *36*, 232–244. [[CrossRef](#)]
42. Xie, Q.; Chen, T.; Zhou, H.; Xu, X.; Xu, H.; Ji, J.; Lu, H.; Balsam, W. Mechanism of palygorskite formation in the red clay formation on the Chinese loess plateau, northwest China. *Geoderma* **2013**, *192*, 39–49. [[CrossRef](#)]
43. Nasedkin, V.V.; Vasiliev, A.L.; Boeva, N.M.; Belousov, P.E. Geology, mineralogy, and genesis of palygorskite clay from Borshchevka deposit in the Kaluga region and outlook for its technological use. *Geol. Ore Depos.* **2014**, *56*, 208–227. [[CrossRef](#)]
44. Mehdilo, A.; Irannajad, M.; Hojjati-rad, M.R. Characterization and beneficiation of iranian low-grade manganese ore. *Physicochem. Probl. Miner. Process.* **2013**, *49*, 725–741. [[CrossRef](#)]
45. Passe-Coutrin, N.; Altenor, S.; Cossement, D.; Jean-Marius, C.; Gaspard, S. Comparison of parameters calculated from the BET and Freundlich isotherms obtained by nitrogen adsorption on activated carbons: A new method for calculating the specific surface area. *Microporous Mesoporous Mater.* **2008**, *111*, 517–522. [[CrossRef](#)]
46. García-Romero, E.; Suárez, M.; Santarén, J.; Alvaréz, A. Crystallochemical characterization of the palygorskite and sepiolite from the Allou Kagne deposit, Senegal. *Clays Clay Miner.* **2007**, *55*, 606–617. [[CrossRef](#)]
47. Presciutti, F.; Capitani, D.; Sgamellotti, A.; Brunetti, B.G.; Costantino, F.; Viel, S.; Segre, A. Electron paramagnetic resonance, scanning electron microscopy with energy dispersion x-ray spectrometry, X-ray powder diffraction, and NMR characterization of iron-rich fired clays. *J. Phys. Chem. B* **2005**, *109*, 22147–22158. [[CrossRef](#)] [[PubMed](#)]

48. Stefaniak, E.A.; Alsecz, A.; Frost, R.; Máthé, Z.; Sajó, I.E.; Török, S.; Worobiec, A.; Grieken, R.V. Combined SEM/EDX and micro-Raman spectroscopy analysis of uranium minerals from a former uranium mine. *J. Hazard. Mater.* **2009**, *168*, 416–423. [[CrossRef](#)]
49. Worobiec, A.; Vermaak, S.P.; Brooker, A.; Darchuk, L.; Stefaniak, E.; Grieken, R.V. Interfaced SEM/EDX and micro-Raman Spectrometry for characterization of heterogeneous environmental particles—Fundamental and practical challenges. *Microchem. J.* **2010**, *94*, 65–72. [[CrossRef](#)]
50. Yang, F.; Sun, S.; Chen, X.; Chang, Y.; Zha, F.; Lei, Z. Mg-Al layered double hydroxides modified clay adsorbents for efficient removal of Pb<sup>2+</sup>, Cu<sup>2+</sup> and Ni<sup>2+</sup> from water. *Appl. Clay Sci.* **2016**, *123*, 134–140. [[CrossRef](#)]
51. Schuette, R.; Goodman, B.A.; Stucki, J.W. Magnetic properties of oxidized and reduced smectites. *Phys. Chem. Miner.* **2000**, *27*, 251–257. [[CrossRef](#)]
52. Mashlan, M.; Bartonkova, H.; Jancik, D.; Tucek, J.; Martinec, P. Iron oxide modified minerals. *Hyperfine Interact.* **2009**, *191*, 151–157. [[CrossRef](#)]
53. Suárez, M.; García-Romero, E. FTIR spectroscopic study of palygorskite: Influence of the composition of the octahedral sheet. *Appl. Clay Sci.* **2006**, *31*, 154–163. [[CrossRef](#)]
54. Cheng, H.; Frost, R.L.; Yang, J.; Liu, Q.; He, J. Infrared and infrared emission spectroscopic study of typical Chinese kaolinite and halloysite. *Spectrochim. Acta Part A Mol. Biomol. Spectrosc.* **2010**, *77*, 1014–1020. [[CrossRef](#)]
55. Lu, Y.; Dong, W.; Wang, W.; Wang, Q.; Hui, A.; Wang, A. A comparative study of different natural palygorskite clays for fabricating cost-efficient and eco-friendly iron red composite pigments. *Appl. Clay Sci.* **2019**, *167*, 50–59. [[CrossRef](#)]
56. Wang, C.; Wang, Z.; Li, C.; Zhen, W.; Wang, S.; Huang, S. Effects of modified palygorskite on performance, crystallization and rheology of polyphenylene sulfide. *Appl. Clay Sci.* **2023**, *240*, 106967. [[CrossRef](#)]
57. Madejová, J. FTIR techniques in clay mineral studies. *Vib. Spectrosc.* **2003**, *31*, 1–10. [[CrossRef](#)]
58. Alkan, M.; Tekin, G.; Namli, H. FTIR and zeta potential measurements of sepiolite treated with some organosilanes. *Microporous Mesoporous Mater.* **2005**, *84*, 75–83. [[CrossRef](#)]
59. Bashir, S.; McCabe, R.W.; Boxall, C.; Leaver, M.S.; Mobbs, D. Synthesis of  $\alpha$ - and  $\beta$ -FeOOH iron oxide nanoparticles in non-ionic surfactant medium. *J. Nanoparticle Res.* **2009**, *11*, 701–706. [[CrossRef](#)]
60. Cheng, H.; Yang, J.; Frost, R.L.; Wu, Z. Infrared transmission and emission spectroscopic study of selected Chinese palygorskites. *Spectrochim. Acta Part A Mol. Biomol. Spectrosc.* **2011**, *83*, 518–524. [[CrossRef](#)]
61. Lazarević, S.; Janković-Castvan, I.; Djokić, V.; Radovanović, Z.; Janačković, D.; Petrović, R. Iron-modified sepiolite for Ni<sup>2+</sup> sorption from aqueous solution: An equilibrium, kinetic, and thermodynamic study. *J. Chem. Eng. Data* **2010**, *55*, 5681–5689. [[CrossRef](#)]
62. Liu, Q.; Yao, X.; Cheng, H.; Frost, R.L. An infrared spectroscopic comparison of four Chinese palygorskites. *Spectrochim. Acta Part A Mol. Biomol. Spectrosc.* **2012**, *96*, 784–789. [[CrossRef](#)]
63. Liu, H.; Chen, T.; Chang, D.; Chen, D.; Qing, C.; Xie, J.; Frost, R.L. The difference of thermal stability between Fe-substituted palygorskite and Al-rich palygorskite. *J. Therm. Anal. Calorim.* **2013**, *111*, 409–415. [[CrossRef](#)]
64. Middea, A.; Spinelli, L.S.; Souza Jr, F.G.; Neumann, R.; Fernandes, T.L.A.P.; Gomes, O.F.M. Preparation and characterization of an organo-palygorskite-Fe<sub>3</sub>O<sub>4</sub> nanomaterial for removal of anionic dyes from wastewater. *Appl. Clay Sci.* **2017**, *139*, 45–53. [[CrossRef](#)]
65. Song, X.; Hao, Y.; Gao, Q.; Cheng, L. Preparation and performance of magnetic zirconium-iron oxide nanoparticles loaded on palygorskite in the adsorption of phosphate from water. *Quim. Nova* **2022**, *45*, 1214–1222. [[CrossRef](#)]
66. Boudriche, L.; Calvet, R.; Hamdi, B.; Balard, H. Surface properties evolution of attapulgite by IGC analysis as a function of thermal treatment. *Colloids Surfaces A Physicochem. Eng. Asp.* **2012**, *399*, 1–10. [[CrossRef](#)]
67. Ogorodova, L.; Vígassina, M.; Melchakova, L.; Krupskaya, V.; Kiseleva, I. Thermochemical study of natural magnesium aluminum phyllosilicate: Palygorskite. *J. Chem. Thermodyn.* **2015**, *89*, 205–211. [[CrossRef](#)]
68. Silva, V.C.; Araújo, M.E.B.; Rodrigues, A.M.; Vitorino, M.B.C.; Cartaxo, J.M.; Menezes, R.R.; Neves, G.A. Adsorption Behavior of Crystal Violet and Congo Red Dyes on Heat-Treated Brazilian Palygorskite: Kinetic, Isothermal and Thermodynamic Studies. *Materials* **2021**, *14*, 5688. [[CrossRef](#)] [[PubMed](#)]
69. Middea, A.; Spinelli, L.S.; Souza Junior, F.G.; Neumann, R.; Fernandes, T.; Faulstich, F.R.L.; Gomes, O. Magnetic polystyrene-palygorskite nanocomposite obtained by heterogeneous phase polymerization to apply in the treatment of oily waters. *J. Appl. Polym. Sci.* **2018**, *135*, 46162. [[CrossRef](#)]
70. Cui, J.; Zhang, Z.; Han, F. Effects of pH on the gel properties of montmorillonite, palygorskite and montmorillonite-palygorskite composite clay. *Appl. Clay Sci.* **2020**, *190*, 105543. [[CrossRef](#)]
71. Subrahmanyam, T.V.; Monte, M.B.M.; Middea, A.; Valdiviezo, E.; Lins, F.F. Contact angles of quartz by capillary penetration of liquids and captive bubble techniques. *Miner. Eng.* **1999**, *12*, 1347–1357. [[CrossRef](#)]
72. Giles, C.H.; MacEwan, S.N.; Nakhwa, S.N.; Smith, D. Studies in Adsorption: Part XI. A System of Classification of Solution Adsorption Isotherms and Its Use in Diagnosis of Adsorption Mechanisms and in Measurement of Specific Surface AREAS of solids. *J. Chem. Soc.* **1960**, *14*, 3973–3993. [[CrossRef](#)]
73. Al-Futaisi, A.; Jamrah, A.; Al-Rawas, A.; Al-Hanai, S. Adsorption capacity and mineralogical and physico-chemical characteristics of Shuwaymiyah palygorskite (Oman). *Environ. Geol.* **2007**, *51*, 1317–1327. [[CrossRef](#)]

74. He, J.; Hong, S.; Zhang, L.; Gan, F.; Ho, Y.S. Equilibrium and thermodynamic parameters of adsorption of methylene blue onto rectorite. *Fresenius Environ. Bull.* **2010**, *19*, 2651–2656. Available online: <http://dns2.asia.edu.tw/~ysho/YSHO-English/Publications/PDF/Fre%20Env%20Bul19,%202651.pdf> (accessed on 25 May 2022).
75. Cychoz, K.A.; Thommes, M. Progress in the Physisorption Characterization of Nanoporous Gas Storage Materials. *Engineering* **2018**, *4*, 559–566. [[CrossRef](#)]

**Disclaimer/Publisher’s Note:** The statements, opinions and data contained in all publications are solely those of the individual author(s) and contributor(s) and not of MDPI and/or the editor(s). MDPI and/or the editor(s) disclaim responsibility for any injury to people or property resulting from any ideas, methods, instructions or products referred to in the content.